

Article



Journal of Vibration and Control 2021, Vol. 0(0) 1–15
© The Author(s) 2021
Article reuse guidelines:
sagepub.com/journals-permissions
DOI: 10.1177/1077546321999510
journals.sagepub.com/home/jvc

Friction-induced instability and vibration in a precision motion stage with a friction isolator

Jiamin Wang¹, Xin Dong², Oumar R Barry¹, and Chinedum Okwudire²

Abstract

Motion stages are widely used for precision positioning in manufacturing and metrology applications. However, they suffer from nonlinear premotion (i.e. "static") friction, which adversely affects their speed and motion precision. In this article, a friction isolator is used as a simple and robust solution to mitigate the undesirable effects of premotion friction in precision motion stages. For the first time, a theoretical study is carried out to understand the dynamic phenomena associated with using a friction isolator on a motion stage. Theoretical analysis and numerical simulation are conducted to examine the dynamical effects of friction isolator on a proportional—integral—derivative-controlled motion stage under LuGre friction dynamics. The influence of friction isolator on the response and stability of the system is examined through theoretical and numerical analyses. Parametric analysis is also carried out to study the effects of friction isolator and friction parameters on the eigenvalue and stability characteristics. The numerical results validate the theoretical findings and demonstrate several other interesting nonlinear phenomena associated with the introduction of friction isolator. This motivates deeper nonlinear dynamical analyses of friction isolator for precision motion control.

Keywords

Precision motion stage, friction isolator, friction-induced vibration, proportional-integral-derivative controller, LuGre friction model, stability analysis

I. Introduction and background

Motion stages are used for precision positioning in a wide range of manufacturing- and metrology-related processes, such as machining, additive manufacturing, and semiconductor fabrication (Altintas et al., 2011). Mechanical bearings (e.g. sliding and especially rolling bearings) are popular in precision motion stages due to their large motion range, high off-axis stiffness, and cost-effectiveness (Altintas et al., 2011). Premotion friction is a common problem encountered in mechanical bearing-based motion stages. The adverse effects in performance caused by premotion friction feature large tracking errors, long settling times, and stick-slip phenomena (Armstrong-Hélouvry et al., 1994; Al-Bender and Swevers, 2008; Futami et al., 1990; Marques et al., 2016). In practice, a common servo feedback controller for precision motion stages is the proportional-integral-derivative (PID) controller (Hensen et al., 2003; Kim and Kim, 2011). While the PID controller is designed to reduce tracking error, the implementation of feedback controllers in the frictional system may result in self-excited limit cycles known as friction-induced vibrations (Duffour and Woodhouse, 2004; Hensen et al., 2003; Hinrichs et al., 1998; Hoffmann, 2007; Hoffmann et al., 2002; Kruse et al., 2015; Nakano and Maegawa, 2009; Niknam and Farhang, 2019; Oestreich et al., 1996; Pascal, 2017; Saha and Wahi, 2011; Van de Vrande et al., 1999), which will further afflict the control performance.

In many studies, the compensation of unwanted frictional effects was realized with different controllers. The traditional high-gain PID controller possesses some robustness and can quickly overcome frictional effects, but it may also lead to large overshoots and limit cycles

¹Department of Mechanical Engineering, Virginia Tech, Blacksburg, VA, USA

 $^2\mbox{Department}$ of Mechanical Engineering, University of Michigan, Ann Arbor, MI, USA

Received: 4 August 2020; accepted: 11 February 2021

Corresponding author:

Oumar R Barry, Department of Mechanical Engineering, Virginia Tech, I307 N Main, Blacksburg 24060, VA, USA.

Email: obarry@vt.edu

(Armstrong-Hélouvry et al., 1994). Robust controllers such as H_{∞} feedback controllers and disturbance observer—based controllers can effectively attenuate model uncertainties and disturbances (Kempf and Kobayashi, 1999; Sariyildiz et al., 2019; Zheng et al., 2017). However, these controllers may be limited in mitigating the highly nonlinear and volatile premotion friction (Chong and Sato, 2010; Kim et al., 2009). Finally, all controllers are affected by practical conditions including computing power, sampling rate, and noise sensitivities, making complex controllers (e.g. neural network controllers (Kim et al., 2009; Ren et al., 2008) less favorable in the application.

The friction isolator (FI), also known as the compliant joint, is a mechanical device recently proposed to effectively and robustly mitigate premotion friction (Dong et al., 2017; Dong and Okwudire, 2018). Unlike the rigid connection (i.e. high stiffness) between mechanical bearings and tables as in the conventional motion stages, FI introduces a lower stiffness between the bearing and the table, which isolates the frictional dynamics and makes the table more compliant in the motion direction. Prior works experimentally demonstrated that with the implementation of FI, the compliant motion stage greatly reduced tracking errors, significantly improved robustness toward friction changes (Dong et al., 2017), and notably shortened settling time compared with the conventional motion stage (i.e. without FI) (Dong and Okwudire, 2018).

Given the remarkable improvements in positioning precision, quickness, and robustness brought by the FI as observed in experiments (Dong et al., 2017; Dong and Okwudire, 2018), it is important to fundamentally understand the beneficial and potentially harmful dynamical effects the FI introduces into the precision motion stage. The conventional motion stage is often modeled as a singlebody friction oscillator. The dynamics in single-body friction oscillators have been extensively investigated in these works, which feature analyses of stability (Hinrichs et al., 1998; Hoffmann, 2007; Kruse et al., 2015; Oestreich et al., 1996; Saha and Wahi, 2011), mode coupling (Hoffmann, 2007; Hoffmann et al., 2002, nonlinear behavior Feeny and Liang, 1997; Hinrichs et al., 1998; Kruse et al., 2015; Oestreich et al. 1996; Saha and Wahi, 2011; Van de Vrande et al., 1999), and bifurcation (Di Bernardo et al., 2003; Hinrichs et al., 1998; Oestreich et al., 1996; Saha and Wahi, 2011; Van de Vrande et al., 1999). Implementing FI will introduce new inertia, stiffness, and damping elements into the system. Studies have also been conducted on the friction-induced vibration of multibody systems (Duffour and Woodhouse, 2004; Galvanetto, 1999; Nakano and Maegawa, 2009; Niknam and Farhang, 2019; Pascal, 2017). However, these works either have not considered premotion frictional dynamics, or they have adopted models that do not fit with the FI-equipped motion stage system. Furthermore, while the effect of the integral controller on the frictional dynamics of single-body systems has been

investigated (Bisoffi et al., 2017; Hensen et al., 2003), none of the studies has explored the frictional behavior of a PID-controlled internally coupled multibody slider system. These problems are investigated for the first time in this article. The aim is to understand the frictional dynamics of a PID-controlled motion stage system with and without FI under matching parameter conditions. As an extension of our conference paper (Dong et al., 2019), the dynamic models are established for PID-controlled motion stages both with and without FI coupled with the LuGre friction model, whose system parameters are experimentally obtained. Numerical simulations are carried out to validate the theoretical analyses. Parametric studies are conducted to understate the role of PID control gains, friction parameters, and FI design parameters on the stability of the motion stage.

The remaining contents of the article are organized as follows: we first establish and discuss the dynamical models of the PID-controlled stages with and without FI under LuGre friction. Next, the linear analysis of the models is carried out by studying the properties of the state Jacobian matrices. We then validate the findings and parametrically study the effect of LuGre friction and FI on the performance and stability of PID-controlled motion stages through both analytical and numerical approaches. Finally, we summarized our findings and propose future works in the conclusion section.

2. Dynamical modeling of motion stages with friction

This section introduces the dynamical modeling of the servo-controlled motion stage systems both with and without FI. For simplicity of labeling, the motion stage without FI is referred to as System α , and the motion stage with FI is referred to as System β hereinafter.

Figure 1(a) shows the schematics of a servo-controlled conventional motion stage without FI (System α). The mass of the moving table rigidly connected to the bearing is $m_t + m_b$, where $m_t > 0$ and $m_b > 0$ are the table mass and the bearing mass, respectively. The table is coupled with the reference command r by stiffness k_p and damping k_d , which are, respectively, equivalent to the proportional and derivative gains of the servo feedback controller that regulate the table position q_t . A supplemental control force u_s is added to account for additional servo forces (e.g. feedforward force and integral controller) that may be applied to the table. The friction force f_f is directly applied to the table via a moving platform at velocity v_p .

The compliant motion stage with FI (System β) is modeled as a system of two coupled oscillators as depicted in Figure 1(b). While System β is largely similar to System α , the newly introduced FI connects the table and the bearing via the stiffness $k_{\rm FI}$ and damping $c_{\rm FI}$, respectively, resulting in the internal coupling between the two bodies. The positions of the table and the bearing are q_t and q_b ,

respectively. The friction force f_f acting on the bearing is not directly applied to the table.

2.1. The LuGre friction model

A variety of friction models have been proposed in the past decades. In this study, the LuGre friction model (De Wit et al., 1995; Hoffmann, 2007) is adopted, which incorporates viscous friction, premotion friction (i.e. presliding/pre-rolling), and hysteresis behaviors. The LuGre model introduces an internal state z, which is used to represent the average deflection of the contact bristles between two surfaces at the friction interface. The dynamics of z are given by

$$\dot{z} = v - a_z(v)z\tag{1}$$

With

$$a_z(v) = \frac{|v|}{g(v)}; \quad g(v) = \frac{f_C + (f_S - f_C)e^{-(v/v_S)^2}}{\sigma_0}$$
 (2)

Where v is the relative velocity between two moving surfaces, f_C is the Coulomb friction, f_S is the static friction, v_s is the Stribeck velocity threshold, and σ_0 is the initial contact stiffness of the bristle. The modeled friction force of the LuGre model is then calculated as

$$f_f = \sigma_0 z + \sigma_1 \dot{z} + \sigma_2 v \tag{3}$$

where σ_1 is the micro-damping of the bristle and σ_2 accounts for the macroscopic viscous friction.

Observe that the dynamics of z are only affected by v. Hence, the equilibrium points of z can be reached only when

(1):
$$v = 0$$
 or (2): $z = \frac{v}{a_z(v)}$ (4)

Equilibrium (1) is known as the sticking equilibrium, and equilibrium (2) is referred to as the slipping equilibrium. The fixed points of any dynamic systems that involve the LuGre friction have to satisfy either of these two conditions. It should be noted that the dynamical model is a switched system at v = 0 due the existence of sgn(v) and |v|.

2.2. Connections between servo-controlled stage and self-excited friction oscillator

As discussed before, the models shown in Figure 1 are often used to study the dynamics of a servo-controlled motion stage during trajectory tracking application, assuming $r \neq 0$ and $v_p = 0$. In this case, the moving table of the stage (i.e. q_t) is controlled to follow a time-varying reference signal r(t). The resulting tracking error can be obtained as

$$\epsilon = q_t - r(t) \tag{5}$$

When the industrial standard linear PID controller is implemented, the feedback control force can be written as

$$u_b = -\epsilon_i - k_p \epsilon - k_d \dot{\epsilon} \tag{6}$$

where $\epsilon_i = k_i \int \epsilon dt$; and k_p , k_i , and $k_d \ge 0$ are respectively the proportional, integral, and derivative gains. If we denote $y_i = k_i \int q_t dt$ as the additional state brought about by the integral action, the full states of the systems are defined as

$$\mathbf{x}_{a} = \begin{bmatrix} q_{t} & \dot{q}_{t} & z & y_{i} \end{bmatrix}^{\mathrm{T}} \tag{7a}$$

$$\mathbf{x}_{\beta} = \begin{bmatrix} q_t & q_b & \dot{q}_t & \dot{q}_b & z & y_i \end{bmatrix}^{\mathrm{T}} \tag{7b}$$

And the state equations of the systems with and without FI are given by

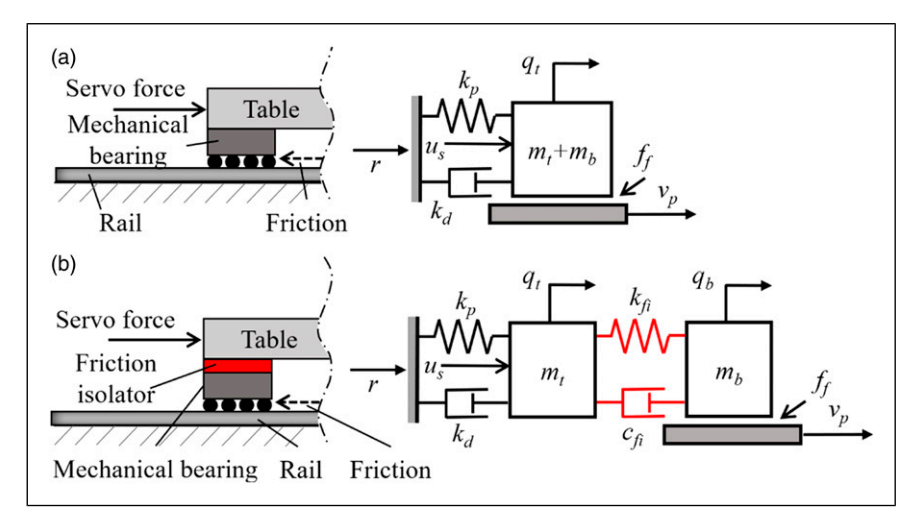


Figure 1. Schematics of servo-controlled motion stage under friction - (a) system α : the conventional motion stage without FI; and (b) system β : the compliant motion stage with FI. Note: FI: friction isolator.

$$\dot{\mathbf{x}}_{\alpha} = \begin{bmatrix} \dot{q}_{t} \\ \frac{(-f_{f} + u)}{m_{\alpha}} \\ v - a_{z}(v) \\ k_{i}q_{t} \end{bmatrix}; \quad \dot{\mathbf{x}}_{\beta} = \begin{bmatrix} \dot{q}_{t} \\ \dot{q}_{b} \\ \frac{(f_{\mathrm{FI}} + u)}{(m_{t})} \\ \frac{(-f_{\mathrm{FI}} - f_{f})}{(m_{b})} \\ v - a_{z}(v) \\ k_{i}q_{t} \end{bmatrix}$$
(8)

Where

$$f_{\rm FI} = k_{\rm FI}(q_b - q_t) + c_{\rm FI}(\dot{q}_b - \dot{q}_t)$$
 (9)

Is the coupling force of the friction isolator, $m_{\alpha} = m_t + m_b$ is the total mass of the system, and u is the additional control input (e.g. feedforward action). The above state equations can be rearranged to obtain the error dynamics as

$$\dot{\mathbf{x}}_{\alpha}^{\star} = \begin{bmatrix} \dot{\epsilon} \\ \frac{(-f_f + u)}{m_{\alpha}} - \ddot{r} \\ v - a_z(v) \\ k_i \epsilon \end{bmatrix}$$
 (10a)

$$\dot{\mathbf{x}}_{\beta}^{\star} = \begin{bmatrix} \dot{\epsilon} \\ \dot{\epsilon}_{b} \\ \frac{(f_{\text{FI}} + u)}{m_{t}} - \ddot{r} \\ \frac{(-f_{\text{FI}} - f_{f})}{m_{b}} - \ddot{r} \\ v - a_{z}(v) \\ k \cdot \epsilon \end{bmatrix}$$
(10b)

Where

$$\mathbf{x}_{\alpha}^{\star} = \begin{bmatrix} \epsilon & \dot{\epsilon} & z & \epsilon_i \end{bmatrix}^{\mathrm{T}} \tag{11a}$$

$$\mathbf{x}_{\beta}^{\bigstar} = \begin{bmatrix} \epsilon & \epsilon_b & \dot{\epsilon} & \dot{\epsilon}_b & z & \epsilon_i \end{bmatrix}^{\mathrm{T}} \tag{11b}$$

$$\epsilon_b = q_b - r \tag{11c}$$

In the literature of friction-induced vibrations under self-excitation (Hinrichs et al., 1998; Hoffmann, 2007; Li et al., 2016; Saha et al., 2016), friction is often introduced by fixing the reference and prescribing the platform (e.g. belt and conveyor) with constant velocity motion (i.e. r = 0, $v_p \neq 0$, and $\dot{v}_p = 0$), as shown in Figure 1. Therefore, the relative velocity v between the frictional interfaces can be written as

$$v_{\alpha} = \dot{q}_t - v_p; \quad v_{\beta} = \dot{q}_b - v_p \tag{12}$$

In the case of servo-controlled motion stage (i.e. $r \neq 0$ and $v_p = 0$), the relative velocities are obtained as

$$v_{\alpha} = \dot{q}_t = \dot{\epsilon} + v_r; \quad v_{\beta} = \dot{q}_b = \dot{\epsilon}_b + v_r$$
 (13)

Note that by substituting r = 0 in equation (12) (i.e., $\dot{q}_t = \dot{\epsilon}$ and $\dot{q}_b = \dot{\epsilon}_b$) and setting $v_r = \dot{r} = -v_p$ (i.e. reference trajectory is constant velocity motion) in equation (13), the relative velocities of these two cases become identical. This indicates that the dynamical response and stability of self-excited friction oscillator and servo-controlled motion stage are equivalent. Even when $\ddot{r} \neq 0$, the equivalence can be acquired simply by designing the controller u as

$$u = u_f + u_b; \quad u_f = m_a \ddot{r} \tag{14}$$

where u_f is the feedforward controller that provides the acceleration. Therefore, in the rest of this article, we will focus on the representation pertaining to the servo-controlled motion stage.

3. Linear stability analysis

The introduction of FI to the servo-controlled motion stage may pose challenges to the stability of the system. In this section, the effects of FI and friction parameters on the feedback controller design of the stage are investigated using linear stability analysis.

3.1. Equilibrium points and state Jacobian matrices

As part of the stability analysis, the calculation of the state equilibrium points may vary with the state representations of the system. For Systems α and β , the equilibrium is studied with respect to the error dynamics (equations (10a, b)) and controller dynamics (equation (6)). As mentioned in the previous section, the equilibrium of the system with the LuGre friction can be reached only when either of the two conditions in equation (4) is satisfied. When the proportional–derivative controller is applied ($k_i = 0$), the stick equilibrium points (at $v_r = 0$) are calculated as

$$\mathbf{x}_{a,0}^{\star} = \begin{bmatrix} \epsilon_0 & 0 & -\frac{k_p \epsilon_0}{\sigma_0} & 0 \end{bmatrix}^{\mathrm{T}}$$
 (15a)

$$\mathbf{x}_{\beta,0}^{\star} = \begin{bmatrix} \epsilon_0 & \frac{(k_t \epsilon_0 - m_b \ddot{r})}{k_{\text{FI}}} & 0 & 0 & -\frac{k_p \epsilon_0}{\sigma_0} & 0 \end{bmatrix}^{\text{T}}$$
(15b)

where $k_t = k_p + k_{\rm FI}$; and $\epsilon_0 \in \mathbb{R}$ is the steady-state position error. When $k_i \neq 0$, the sticking equilibrium points become

$$\mathbf{x}_{a,0}^{\star} = \begin{bmatrix} 0 & 0 & -\frac{\epsilon_{i,0}}{(\sigma_0)} & \epsilon_{i,0} \end{bmatrix}^{\mathrm{T}}$$
 (16a)

$$\mathbf{x}_{\beta,0}^{\star} = \begin{bmatrix} 0 & \frac{(\epsilon_{i,0} - m_b \ddot{r})}{k_{\text{FI}}} & 0 & 0 & -\frac{\epsilon_{i,0}}{\sigma_0} & \epsilon_{i,0} \end{bmatrix}^{\text{T}}$$
 (16b)

where $\epsilon_{i,0} \in \mathbb{R}$ is the integral error that balances the unmodeled system dynamics.

The slipping equilibrium occurs when $v_r \neq 0$. In the absence of integral action (i.e. PD control), the equilibrium points are obtained as

$$\mathbf{x}_{a,0}^{\star} = \begin{bmatrix} -\frac{f_{f,0}}{k_p} \\ 0 \\ h(v_r) \\ 0 \end{bmatrix}; \quad \mathbf{x}_{\beta,0}^{\star} = \begin{bmatrix} -\frac{f_{f,0}}{k_p} \\ \epsilon_{b,0,pd} \\ 0 \\ h(v_r) \\ 0 \end{bmatrix}$$
(17)

Where

$$h(v) = \frac{v}{a_z(v)} = \operatorname{sgn}(v)g(v)$$

$$f_{f,0} = \sigma_0 \ h(v_r) + \sigma_2 v_r$$

$$\epsilon_{b,0,pd} = -\frac{\left(k_t f_{f,0} + k_p m_b \ddot{r}\right)}{\left(k_p k_{\text{FI}}\right)}$$

Similarly, the slipping equilibrium points in the presence of PID controllers can be calculated as

$$\mathbf{x}_{a,0}^{\star} = \begin{bmatrix} 0 \\ 0 \\ h(v_r) \\ -f_{f,0} \end{bmatrix}; \quad \mathbf{x}_{\beta,0}^{\star} = \begin{bmatrix} 0 \\ -\frac{(f_{f,0} + m_b \ddot{r})}{k_{FI}} \\ 0 \\ 0 \\ h(v_r) \\ -f_{f,0} \end{bmatrix}$$
(18)

Linear stability analysis is carried out by examining the Hurwitz properties of the state Jacobian matrix, which is obtained by linearizing the system around the equilibrium points (Khalil, 2002; Ogata, 2010). To make sure that the steady-state solution of a nonlinear system locally converges to a fixed point, it is necessary for the linearized system at the fixed point to be stable. The sticking equilibrium assumes $v_r = 0$, which is not relevant to the scope of this article. Therefore, the stability analysis is conducted at the slipping equilibrium points. For System α and $k_i = 0$, the state Jacobian matrix is

$$\mathbf{A}_{\alpha} = \begin{bmatrix} 0 & 1 & 0 \\ -\frac{k_p}{m_a} & a_{a,[2,2]} & a_{a,v,z} \\ 0 & a_{a,z,v} & -a_z(v) \end{bmatrix}$$
(19)

With

$$a_{a,[2,2]} = -\frac{(k_d + \sigma_1 + \sigma_2 - \sigma_1 z(\partial a_z(v)/\partial v))}{m_a}$$
 (20a)

$$a_{\alpha,\nu,z} = -\frac{(\sigma_0 - \sigma_1 a_z(\nu))}{m_\alpha} \tag{20b}$$

$$a_{a,z,v} = 1 - z \left(\frac{\partial a_z(v)}{\partial v} \right)$$
 (20c)

Where

$$\frac{\partial a_z(v)}{\partial v} = \frac{\operatorname{sgn}(v) \left[g(v) v_s^2 + 2v^2 (g(v) - f_C / \sigma_0) \right]}{g^2(v) v_s^2} \tag{21}$$

Because z = h(v) at the equilibrium, equations (20a–c) can be further simplified as

$$a_{a,[2,2]} = -\left(\frac{k_d + \sigma_2 - \sigma_1 \rho_f(v)v^2}{v_s^2}\right)$$
 (22a)

$$a_{a,z,v} = -\frac{\rho_f(v)v^2}{v_c^2}$$
 (22b)

Where

$$\rho_f(v) = 2 - \frac{2f_C}{f_C + (f_S - f_C)e^{-(v/v_S)^2}}$$
 (23)

is the ratio bounded by $(0, 2(f_S - f_C)/f_S]$. Similarly, for System β and $k_i = 0$, the Jacobian can be calculated as

$$\mathbf{A}_{\beta} = \begin{bmatrix} 0 & 0 & 1 & 0 & 0 \\ 0 & 0 & 0 & 1 & 0 \\ a_{\beta,[3,1]} & \frac{k_{\text{FI}}}{m_t} & a_{\beta,[3,3]} & \frac{c_{\text{FI}}}{m_t} & 0 \\ \frac{k_{\text{FI}}}{m_b} & -\frac{k_{\text{FI}}}{m_b} & \frac{c_{\text{FI}}}{m_b} & a_{\beta,[4,4]} & a_{\beta,\nu,z} \\ 0 & 0 & 0 & a_{\beta,z,\nu} & -a_z(\nu) \end{bmatrix}$$
(24)

Where

$$a_{\beta,[3,1]} = -\frac{\left(k_{\rm FI} + k_p\right)}{m_{\star}}$$
 (25a)

$$a_{\beta,[3,3]} = -\frac{(c_{\rm FI} + k_d)}{m_t}$$
 (25b)

$$a_{\beta,[4,4]} = -\frac{\left(c_{\text{FI}} + \sigma_2 - \sigma_1 \rho_f(v) v^2 / v_s^2\right)}{m_b}$$
 (25c)

$$a_{\beta,\nu,z} = -\frac{(\sigma_0 - \sigma_1 a_z(\nu))}{m_b} \tag{25d}$$

$$a_{\beta,z,v} = -\frac{\rho_f(v)v^2}{v_s^2}$$
 (25e)

Notice that the sign of v does not affect the values of state Jacobian matrices, thus confirming the symmetry property of the system. These matrices are only dependent on the states $\dot{\epsilon}$ (for System α), $\dot{\epsilon}_b$ (for System β), and z. The resulting values of Jacobian matrices at the slipping equilibrium points are obtained by setting $v = v_r$. For the PID cases, the state Jacobian matrices can be defined as

$$\mathbf{A}_{a,i} = \begin{bmatrix} 0 & \begin{bmatrix} k_i & 0 & 0 \end{bmatrix} \\ \begin{bmatrix} 0 - 1 \\ m_a \end{bmatrix}^{\mathrm{T}} & \mathbf{A}_a \end{bmatrix}$$
 (26)

And

$$\mathbf{A}_{\beta,i} = \begin{bmatrix} 0 & [k_i & 0 & 0 & 0 & 0] \\ 0 & 0 & -\frac{1}{m_t} & 0 & 0 \end{bmatrix}^{\mathsf{T}} \qquad \mathbf{A}_{\beta}$$
(27)

Which are obtained by rearranging the sequence of the states (i.e. moving ϵ_i to the first state).

Finally, it is helpful to convert the dimensional Jacobian matrix to a nondimensional form such that the eigenvalues are scaled for easier comparison. The general procedure is to select a principal natural frequency ω_n and use the corresponding nondimensional time $t_n = \omega_n t$. In this study, the principal natural frequency for the two systems are selected as

$$\omega_{n,\alpha} = \sqrt{\frac{k_p}{m_\alpha}}$$

$$\omega_{n,\beta} = \sqrt{\frac{k_p}{m_t}}$$
(28)

The nondimensional state Jacobian matrices of the systems can then be obtained as

$$\mathbf{A}_{n,a,i} = \mathbf{\Omega}_{n,a,1} \mathbf{A}_{a,i} \mathbf{\Omega}_{n,a,2} \tag{29a}$$

$$\mathbf{A}_{n,\beta,i} = \mathbf{\Omega}_{n,\beta,1} \mathbf{A}_{\beta,i} \mathbf{\Omega}_{n,\beta,2} \tag{29b}$$

Where

$$\mathbf{\Omega}_{n,a,1} = \operatorname{diag}\left(\begin{bmatrix} 1 & \omega_{n,a}^{-1} & \omega_{n,a}^{-2} & \omega_{n,a}^{-1} \end{bmatrix}\right) \tag{30a}$$

$$\mathbf{\Omega}_{n,\alpha,2} = \operatorname{diag}(\begin{bmatrix} \omega_{n,\alpha}^{-1} & 1 & \omega_{n,\alpha} & 1 \end{bmatrix})$$
 (30b)

$$\mathbf{\Omega}_{n,\beta,1} = \operatorname{diag}\left(\begin{bmatrix} 1 & \omega_{n,\beta}^{-1} & \omega_{n,\beta}^{-1} & \omega_{n,\beta}^{-2} & \omega_{n,\beta}^{-2} & \omega_{n,\beta}^{-1} \end{bmatrix}\right)$$
(30c)

$$\mathbf{\Omega}_{n,\beta,2} = \operatorname{diag}(\begin{bmatrix} \omega_{n,\beta}^{-1} & 1 & 1 & \omega_{n,\beta} & \omega_{n,\beta} & 1 \end{bmatrix}) \quad (30d)$$

Note that the stability implied by the nondimensional Jacobian matrices are identical to those from the dimensional matrices.

3.2. Properties of state Jacobian matrices

To guarantee the stability of the linearized system, the state matrix has to be Hurwitz, that is, all eigenvalues have negative real parts. This can be evaluated by directly calculating the eigenvalues or applying the Routh–Hurwitz criterion (Ogata, 2010) on the characteristic equations calculated from the state Jacobian matrices. For example, the characteristic equation of \mathbf{A}_{α} can be calculated as

$$s^3 + b_1 s^2 + b_2 s + b_3 = 0 (31)$$

where the roots of this characteristic equation are the eigenvalues, and

$$b_1 = a_z(v) + \frac{\left[k_d + \sigma_2 - \sigma_1 \rho_f(v) v^2 / v_s^2\right]}{m_a}$$
 (32a)

$$b_{2} = \frac{\left[k_{p} + k_{d}a_{z}(v) + \sigma_{2}a_{z}(v) - \sigma_{0}\rho_{f}(v)v^{2}/v_{s}^{2}\right]}{m_{\alpha}}$$
(32b)

$$b_3 = \frac{a_z(v)k_p}{m_a} \tag{32c}$$

If $b_1b_2 > b_3$, the system is linearly stable. While a complete symbolical evaluation of the Hurwitz property is very difficult due to the complexity of the system, for System α under PD control, it is observed that when $\sigma_0 \to \infty$, other coefficients have trivial effects on the stability of the system. This leads to $b_1 \approx a_z(v)$, and the simplified stability condition can be obtained as

$$b_1 b_2 - b_3 \approx \frac{a_z^2(v)}{m_\alpha^2} \left(k_d + \sigma_2 - \frac{|v|(f_S - f_C)e^{-v/v_s^2}}{v_s^2} \right) > 0$$
(33)

Note that σ_1 is not presented in the above expression. This indicates that micro-damping does not affect system stability when $\sigma_0 \to \infty$. Also, smaller v_s requires larger k_d or σ_2 to stabilize the system, especially when v is close to v_s . In addition, for a fixed v_s , the lower bounds of k_d and σ_2 that stabilize the system reach maximum values when v = v

 $v_s/\sqrt{2}$; this is obtained by taking the derivative of $|v|(f_S - f_C)e^{-(v/v_s)^2}/v_s^2$ with respect to v.

Several other interesting properties of the systems can also be obtained by examining the structure of the Jacobian matrices. Notice that all the matrices can be decomposed into the following structure

$$\mathbf{A} = \begin{bmatrix} \mathbf{A}_{M} & [0 & \dots & 0 & a_{v,z}] \\ [0 & \dots & 0 & a_{z,v}]^{\mathrm{T}} & -a_{z}(v) \end{bmatrix}$$
(34)

where A_M is the submatrix corresponding to the states from the multibody system. For both systems, it can be observed that $\rho_f(v) \to 0$ when $|v| \gg v_s$. As a result, when the relative velocity at friction surface is significantly larger than the Stribeck velocity threshold, $a_{z,v} \rightarrow 0$ and the eigenvalues of **A** consist of eigenvalues of \mathbf{A}_M and $-a_z(v)$, respectively; the latter is negative by default. This indicates that the effects of friction dynamics and multibody dynamics on the system stability are decoupled when the velocity is large. The same conclusion can be drawn when $v_s \gg |v| > 0$ or $f_S \approx$ f_C , which all lead to $a_{z,v} \to 0$. Based on this property, the analysis scope can be reasonably focused on the low speed range (i.e., when v_r is close to v_s). Similarly, the structures of A_i indicate that, when k_i is small, the eigenvalues from A will be unaffected and carried over to A_i . This property makes it convenient to distinguish the eigenvalue introduced by the additional integral state ϵ_i .

4. Results and discussion

In this section, we first validate the theoretical observations using numerical simulation, and then, we examine the effects of LuGre friction and FI on the performance and stability of PID-controlled motion stages. The default design and friction parameters obtained from the prototype in previous experimental studies (Dong et al., 2017; Dong and Okwudire, 2018; Dong et al., 2019) are

$$m_t = 1 \text{ kg}$$

 $m_b = 0.5 \text{ kg}$ (35a)
 $f_S = 6.5 \text{ N}$

$$f_C = 5.1 \text{ N}$$

 $k_{\text{FI}} = 4 \times 10^4 \text{ N/m}$ (35b)
 $c_{\text{FI}} = 2 \text{ Ns/m}$

$$v_s = 16.7 \,\text{mm/s}$$

 $\sigma_0 = 2.2 \times 10^6 \,\text{N/m}$ (35c)

$$\sigma_1 = 237 \text{ Ns/m}$$

 $\sigma_2 = 14.2 \text{ Ns/m}$ (35d)

The default PID controller gains are

$$k_p = 2 \times 10^4 \,\text{N/m}$$

 $k_i = 1 \times 10^6 \,\text{N/ms}$ (36a)

$$k_d = 2 \times 10^2 \,\text{Ns/m}$$
 (36b)

The default reference velocity is chosen as $v_r = 10$ mm/s. The initial conditions of the numerical simulations are selected as $\mathbf{x}_{\alpha}^{\bigstar} = [0, -v_r, 0, 0]^{\mathrm{T}}$ and $\mathbf{x}_{\beta}^{\bigstar} = [0, 0, -v_r, -v_r, 0, 0]^{\mathrm{T}}$.

4.1. Numerical validation of the theoretical results

To validate the results from the linear stability analysis, numerical simulations are first carried out using the built-in ODE solver ode45 in MATLAB with the nonlinear system equations. Constant velocity motion is used as the reference trajectory, that is, $r = v_r t$. The parameters used in the numerical validation are from equations (35a–d) and (36a, b).

It is observed that the numerical stability analysis closely matches with the one obtained analytically. An example carried out on System β is demonstrated in Figure 2, which compares the linear stability regions with the steady-state oscillation amplitudes, respectively, within the k_i - k_p domain and the k_i - k_d domain. The stability regions are calculated by evaluating the Hurwitzness of the state matrix $\mathbf{A}_{\beta,i}$ through eigenvalues. The steady state oscillation amplitudes are calculated by simulating the ODE of System β until the transient responses are phased out.

The analytical results yield a boundary that separates the stable and unstable regions. Although the numerical results do not provide a direct indication of stability, the steady-state solutions of $\mathbf{x}_{\beta}^{\star}$ that converge to zeros (i.e. fixed points) can be separated from the ones with nonzero amplitudes (i.e. oscillations). The separation contours match excellently with the stability boundaries calculated analytically. This is an indication that the stability of the nonlinear system can be reliably evaluated through the analytical approach from the linear analysis, which leads to the following parametric study on the stability of PID-controlled motion stages.

4.2. Effect of friction on system stability

In the servo-controlled motion stage, the PID controller is designed to first stabilize the system. Therefore, the effects of friction on the stability of PID-controlled motion stages are investigated with a focus on how the ranges of stable control gains are affected. As discussed in the modeling section, the LuGre friction force f_f is determined by a total of seven parameters—v, v_s , f_s , f_c , σ_0 , σ_1 , and σ_2 , among which only v is state dependent. Based on the fact that $v = v_r$ at the equilibrium points, the ranges of stable PD control gains (i.e. $k_i = 0$) at the default reference velocity $v_r = 10$ mm/s are compared between System α and β -see Figure 3. It can be observed that a decrease in the stable gain region occurs when FI is applied. Similar observation is also shown in

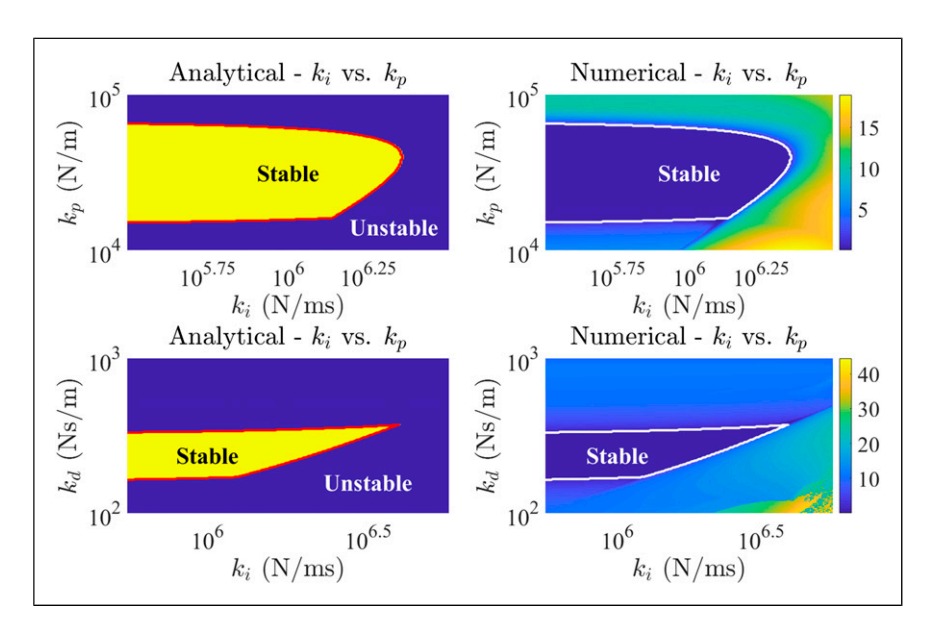


Figure 2. The analytical stability region of proportional-integral-derivative control gains and its corresponding steady state oscillation error amplitude map acquired through the numerical simulation. For analytical results, the stable (light yellow) and unstable (dark blue) regions are separated by the stability boundaries (red); for numerical results, the white contours enclose the steady state solutions that converge to zeros (i.e. fixed points).

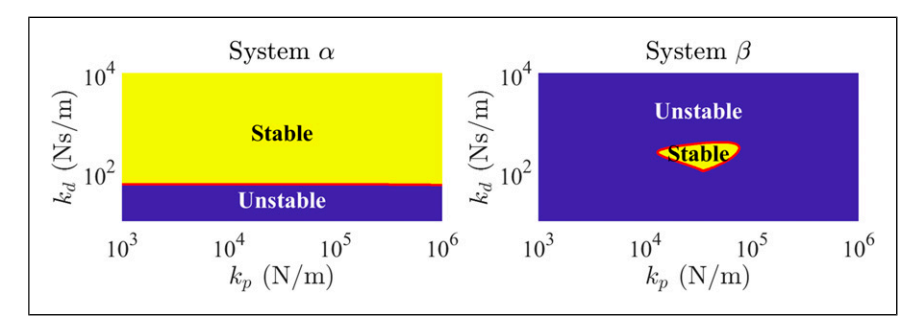


Figure 3. Region of stable proportional–derivative gain for system α and β at $v_r = 10$ mm/s. The stable (light yellow) and unstable domains (dark blue) are separated by the stability boundary (red)

Figure 4, where the variation of the stable gain boundary with different v_r is presented. In general, it is much harder to tune the PD gains that can stabilize System β to the equilibrium point. For System α , the boundary can be predicted by equation (33). The results suggest that k_d needs to be larger than a certain value to overcome the destabilizing effect of friction. It is also observed that at the critical velocity $v_r = v_s/\sqrt{2} \approx 11.8$ mm/s, System α has the smallest stable region. This matches with the finding from equation (33). Although it is harder to obtain such a value for System β , Figure 4 shows that the smallest stable gain boundary also appears around $v_r = v_s/\sqrt{2}$. The following analysis is carried out at $v_r =$ 10 mm/s for simplicity. Notice from Figure 4 that at $v_r =$ 10 mm/s, the stability boundary is close to that from the worst case scenario observed at the critical velocity $v_r = v_s/\sqrt{2}$.

In the presence of integral action, the effects of friction parameters on the ranges of stable control gains are shown in Figure 5. In general, an extremely large k_i leads to instability, which is true for both systems in this study. For system α , increasing k_p and k_d allows the tuning of a larger stable k_i . Note that $k_p(k_d + \sigma_2) > k_i m_\alpha$ is the stability criterion when the LuGre dynamics are decoupled from the rigid-body dynamics (i.e. $|v_r| \gg v_s$ or $v_s \gg |v_r|$). The coupling with friction reduces the stability boundaries in both motion stages (i.e. the orange areas in Figure 5 are subtracted from the original stable region), which is particularly significant for System β . Finally, note that the stability boundaries are hardly affected within the range where k_i is small.

Figure 6 shows the stable k_p - k_d boundaries as the integral gain k_i changes. Observe that the increase of k_i reduces and shifts the stable PD control gain domains for both systems. This indicates that extra care should be taken when using

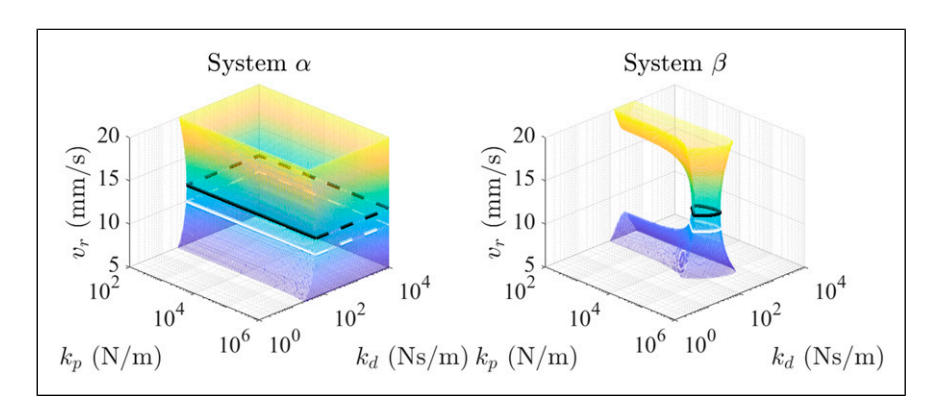


Figure 4. The evolution of the boundary of the stable proportional–derivative gain domain (enclosed by the boundary) with respect to v_r for both systems, where the white contour is the boundary at $v_r = 10$ mm/s (also observable in Figure 3), and the black contour is the boundary at $v_r = v_s / \sqrt{2} \approx 11.8$ mm/s. The dash-line edges indicate the openings of the boundary (i.e. the system does not become unstable with very high k_d gains or k_b gains).

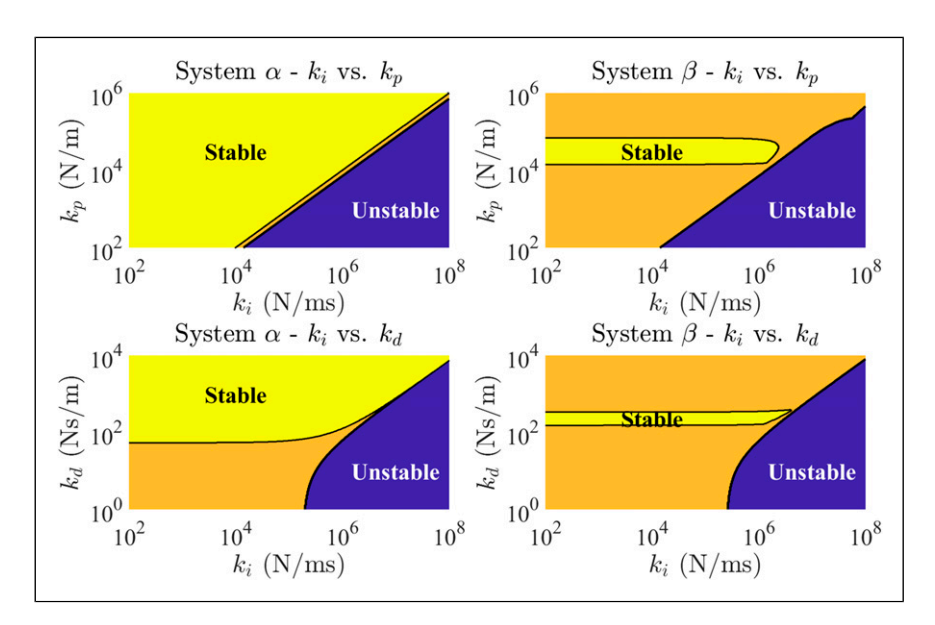


Figure 5. Stability region of system α and β under proportional–integral–derivative control, where: the light yellow areas (marked as stable) indicate stability for both $v_r = 10$ mm/s and $|v_r| \gg v_s$ (i.e. friction dynamics is isolated) cases; the dark blue areas (marked as unstable) indicate instability for both $v_r = 10$ mm/s and $|v_r| \gg v_s$; and the remaining orange areas indicate instability for $v_r = 10$ mm/s but stability when $|v_r| \gg v_s$.

a k_i of large magnitude to quickly overcome the disturbance. For System β , the stability boundaries of the PD control gains are not much affected by the default value of k_i from equations (36a, b) when compared with the PD control case (where $k_i = 0$).

To summarize, the friction can cause instabilities of PID-controlled motion stages both with and without FI. The observations of the effect of the tracking velocity v_r on the stability boundaries corroborate the analytical findings from the previous section. It is also observed that FI, with the default parameters, can further reduce the ranges of stable PID gains for System β . This indicates that the choice of FI

parameters is critical to the controller design and the stability of the motion stage.

4.3. Effect of friction isolator on system stability

An interesting phenomenon observed in the previous subsection is that System β experiences unstable—stable—unstable transition as k_p or k_d increases. This is different from System α , in which stability is guaranteed once k_p or k_d is larger than a critical value. To further investigate this, the trajectories of the eigenvalues of the systems are evaluated using root locus plots. Based on the default

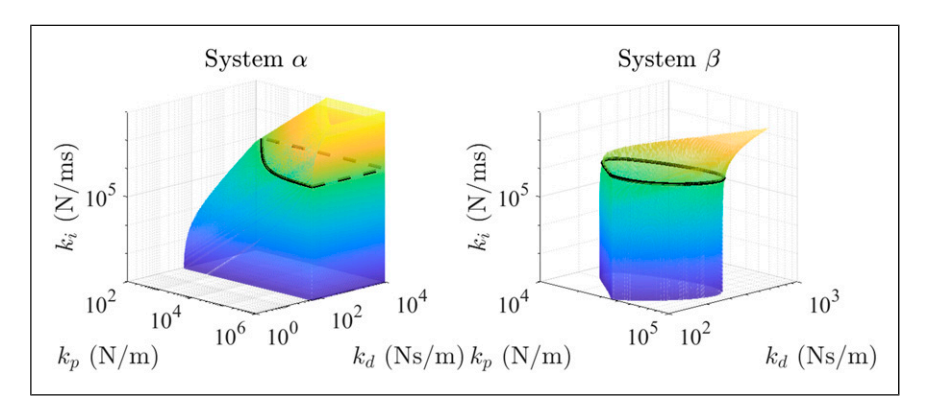


Figure 6. The evolution of the boundary of the stable k_p - k_d domain (enclosed by the boundary) with respect to k_i for both systems, where the black contour is the boundary at the default $k_i = 1 \times 10^6$ N/ms. The dash-line edges indicate the openings of the boundary (i.e. the system does not become unstable with very high k_d gains or k_b gains)

parameters in equations (35a-d) and (36a, b), it is observed that the following eigenvalues are critical to system stability:

- 1. An eigenvalue λ_i (for both systems) introduced by the additional integral state ϵ_i , that is, $\lambda_i = 0$ at $k_i = 0$.
- 2. A negative real eigenvalue λ_z (for both systems) that is introduced by the bristle dynamics with large magnitude.
- 3. Eigenvalues λ_t and λ_b (for System β alone) in complex pairs that are introduced by the table and bearing.

The root locus of System α for the abovementioned eigenvalues is presented in Figure 7. Because λ_z has a very large magnitude compared with the other eigenvalues, its trajectories have been excluded from the plot. The figure demonstrates the transition of system stability from unstable to stable as k_p and k_d increase. Note that for System β , two eigenvalue trajectories (i.e. in blue and red) are very similar to those in the root locus of System α ; they show the same unstable–stable transition as k_p and k_d increases. However, the additional trajectories of the complex eigenvalue pairs (in green) demonstrate the unstable–stable–unstable transition as they both cross the imaginary axis twice. This

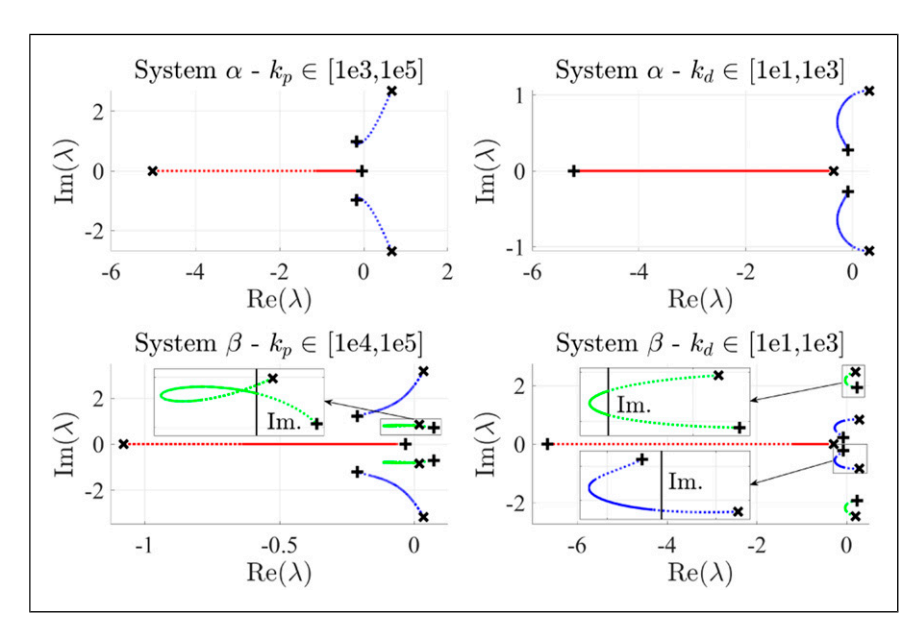


Figure 7. Non-dimensionalized root locus (excluding λ_z) of system α and β with respect to k_p and k_d with $v_r = 10$ mm/s and $k_i = 1 \times 10^6$ N/ms, where: different colors are used to distinguish eigenvalues; the dotted and solid lines indicate the range of the locus where the systems are unstable (i.e. one or more eigenvalues have positive real parts) and stable (i.e. all eigenvalues have negative real parts), respectively; the "x" and "+" markers respectively indicate the beginning and the end of the locus. In the zoomed-in subplots, the black line is the imaginary axis (marked with "lm.").

explains why the presence of FI shrinks the range of k_p and k_d values that can stabilize the system. An explanation of the stable-to-unstable transition in System β is as follows: when k_p and k_d become very large, the table is rigidly "constrained" to the tracking reference, resulting in $q_t \approx r$. This leads to System β being reduced to a one-body system such as System α , where $k_{\rm FI}$ and $c_{\rm FI}$ play the roles of k_p and k_d , respectively. In the current case, $c_{\rm FI}$ is small, which leads to instability of the system due to the frictional effect.

Therefore, it is very important to study the effects of FI parameters on system stability. By defining μ_k , $\mu_c \in \mathbb{R}_+$, the FI stiffness and damping can be scaled as $k_{\rm FI} = \mu_k k_{\rm FI,0}$ and $c_{\rm FI} = \mu_c c_{\rm FI,0}$, respectively where $k_{\rm FI,0}$ and $c_{\rm FI,0}$ are the default values from equation (35a–d). The resulting stable k_p - k_d boundary with respect to different scaling coefficients is shown in Figure 8. The result indicates that increasing $k_{\rm FI}$ and $c_{\rm FI}$ both extend the range of stable PID controller gains. Note that if $k_{\rm FI}$ and $c_{\rm FI}$ are extremely large, the table and bearing will be rigidly connected, which also reduces System β to System α .

Previous results show the change of stable PD regions as the FI parameters vary. Alternatively, the influence of design parameters can be visualized by examining their stable combinations with a fixed set of controller parameters. Two new coefficients μ_t , $\mu_b \in \mathbb{R}_+$ are defined so that the mass of the table and bearing can be scaled as $m_t = \mu_t m_t$, 0 and $m_b = \mu_b m_{b,0}$, respectively. The corresponding stability charts in the $\mu_k - \mu_c$ and $\mu_t - \mu_b$ domains are shown in Figure 9 with the default controller gains. Similar to the previous analysis, it is observed that the stability is improved by increasing $k_{\rm FI}$ and $c_{\rm FI}$. The results on μ_t and μ_b show that the range of stable m_t - m_b combinations is quite narrow due to the introduction of FI. This may limit the payload that a motion stage can handle in practice. This problem may be alleviated by increasing the FI damping $c_{\rm FI}$ or adopting smaller integral gain k_t as shown in Figure 10.

In summary, the choice of FI parameters is essential to the stability of the system. There is a trade-off between better isolation performance (in terms of mitigating undesirable effects of premotion friction) and improved system stability (in terms of stable regions of PID controller gains) (Dong et al., 2017; Dong and Okwudire, 2018). The linear stability analyses from this section can serve as useful guidelines during the design optimizations of FI.

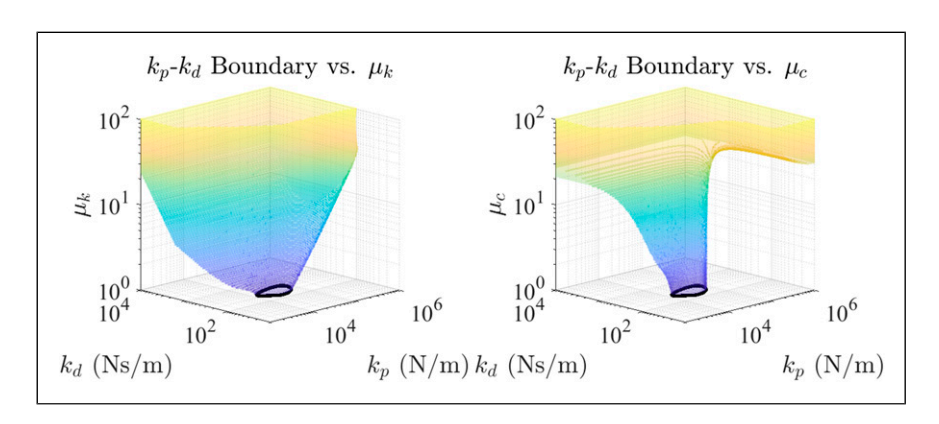


Figure 8. The development of boundary of the stable k_p - k_d region (enclosed by the boundary) with respect to μ_k and μ_c for system β with $v_r = 10$ mm/s and $k_i = 1 \times 10^6$ N/ms, where the black contours are the boundary with the default parameters.

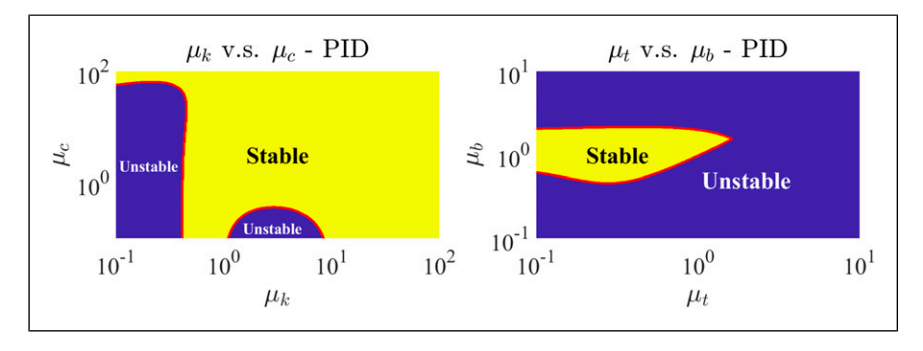


Figure 9. Stability of the system at different design parameters with the default proportional–integral–derivative gains and v_r defined in equation (36a, b), where stable (light yellow) and unstable (dark blue) domains are separated by the stability boundaries (red)

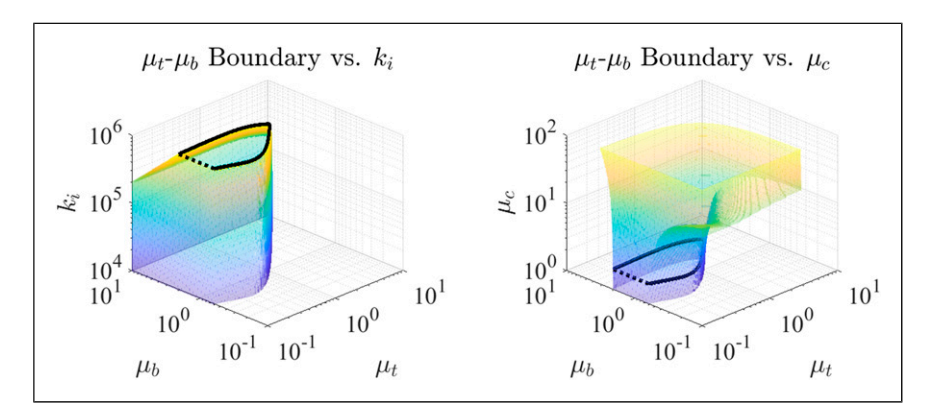


Figure 10. The evolution of the boundary of stable μ_t - μ_b range (enclosed by the boundary) with respect to k_i and μ_c , where the black contours are the boundary with the default parameters observable from Figure 9. The dot-line edges indicate the openings of boundary (i.e. smaller μ_t will not lead to instability).

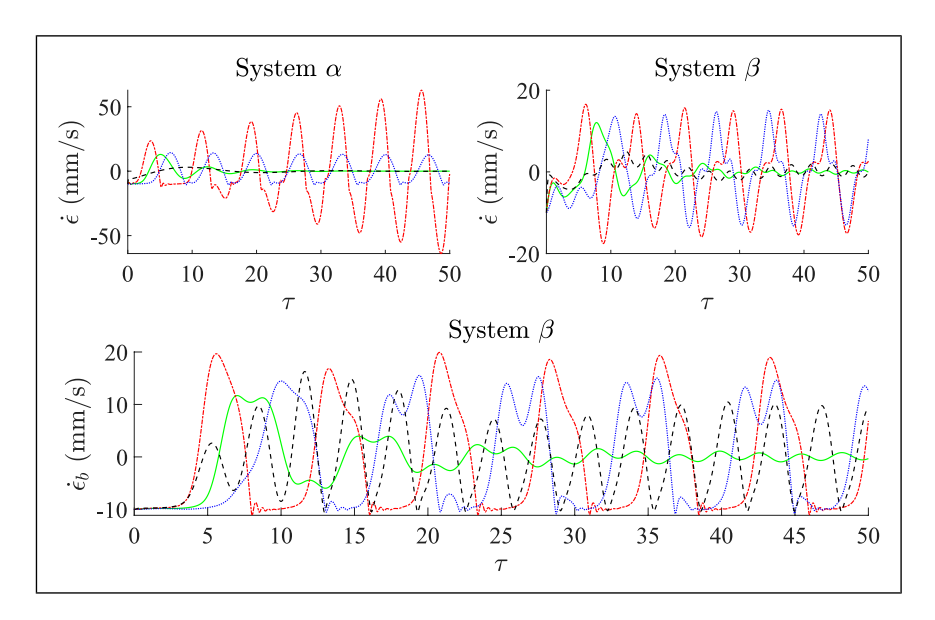


Figure 11. Comparison of velocity error time trajectories ($v_r = 10 \text{ mm/s}$) with different k_i and k_d for System α and β , where (1) solid default gains in Equations (36a, b), (2) dot - change in $k_i = 4.5 \times 10^6 \text{ N/ms}$, (3) dash-dot - changes in $k_i = 1 \times 10^5 \text{ N/ms}$ and $k_d = 20 \text{ Ns/m}$, (4) dash - change in $k_d = 1 \times 10^3 \text{ Ns/m}$.

4.4. Effect of FI on the limit cycle amplitude of the motion stage

This subsection examines the role of the FI on the limit cycle amplitude of the motion stage using numerical simulations. Figure 11 shows the time domain data of $\dot{\epsilon}$ and $\dot{\epsilon}_b$ with different controller gains (i.e., k_i and k_d). Note that nondimensional time $t_n = \omega_n t$ is used to provide a good time span for observation. For both Systems α and β , cases (2) and (3) are unstable. However, two types of instability are observed for System α : the instability in case (2) is caused by an extremely large k_i that eventually leads $\dot{\epsilon}$ to infinity; the instability in case (3) is the stick–slip phenomenon caused by the initial instability of the PD controller as

a result of the coupling between friction dynamics and multibody dynamics (i.e., refer to the stability region in Figure 3). Although the ranges of stable PID gains are reduced in the presence of the FI, case (2) indicates that the implementation of the FI may prevent the error from going unbounded. In addition, while a large k_d causes instability for System β as shown in case (4), it can be observed that the corresponding $\dot{\epsilon}$ has very small oscillation amplitude which may not affect the precision of the motion stage in practice.

The simulated velocity errors using different design parameter scaling factors are shown in Figure 12. In general, the system stability with different combinations of design parameters is well predicted by the linear analysis. Interestingly, the unstable oscillation in case (4) does not show

any pattern of stick–slip, even though the instability is related to the coupling between friction dynamics and multibody dynamics. The numerical results from different μ_t and μ_b combinations in Figure 12 match with the observation in Figure 10, which shows that the system stability is very sensitive to the change of masses in the presence of

FI because only case (4) is stable with the choice of scaling factors between 0.5 and 2.

The above numerical results show that the majority of the instability behaviors are bounded, indicating the existence of limit cycles. Existing literature (Johanastrom and Canudas-De-Wit, 2008; Saha et al., 2016) has studied the

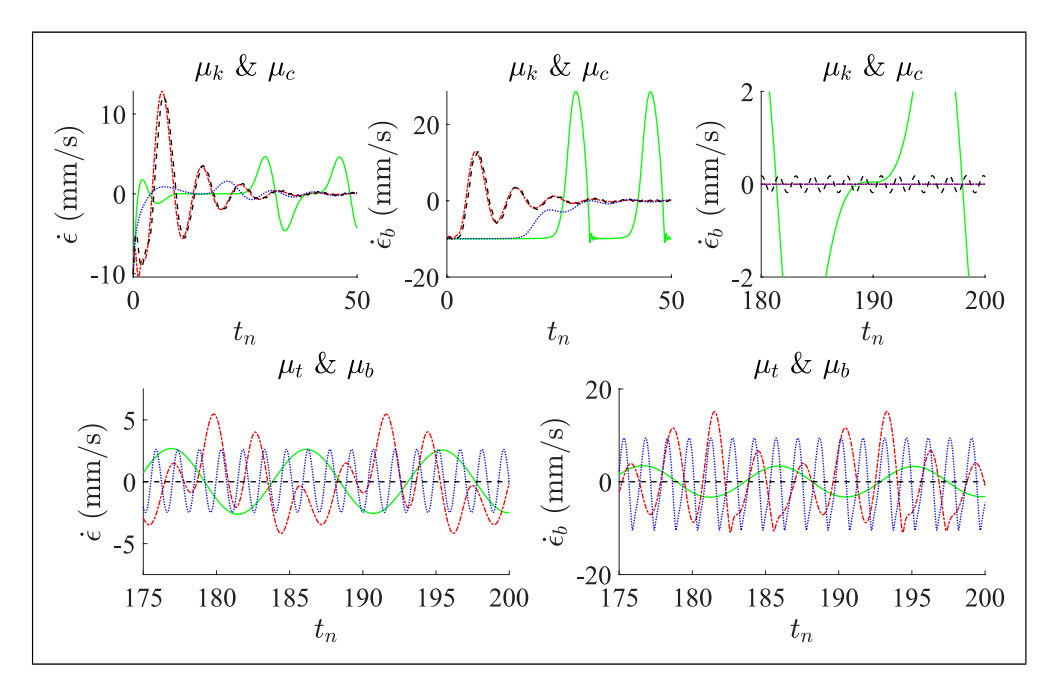


Figure 12. Comparison of velocity error time trajectories ($v_r = 10$ mm/s) with different scaling factors μ , where for $\mu_k \& \mu_c$: (1) solid - $\mu_k = 0.1$, (2) dot - $\mu_k = 10$, (3) dash-dot - $\mu_k = 0.1$ and $\mu_c = 100$, (4) dash - $\mu_k = 0.25$; and for $\mu_t \& \mu_b$: (1) solid - $\mu_b = 0.5$, (2) dot - $\mu_t = 0.5$.

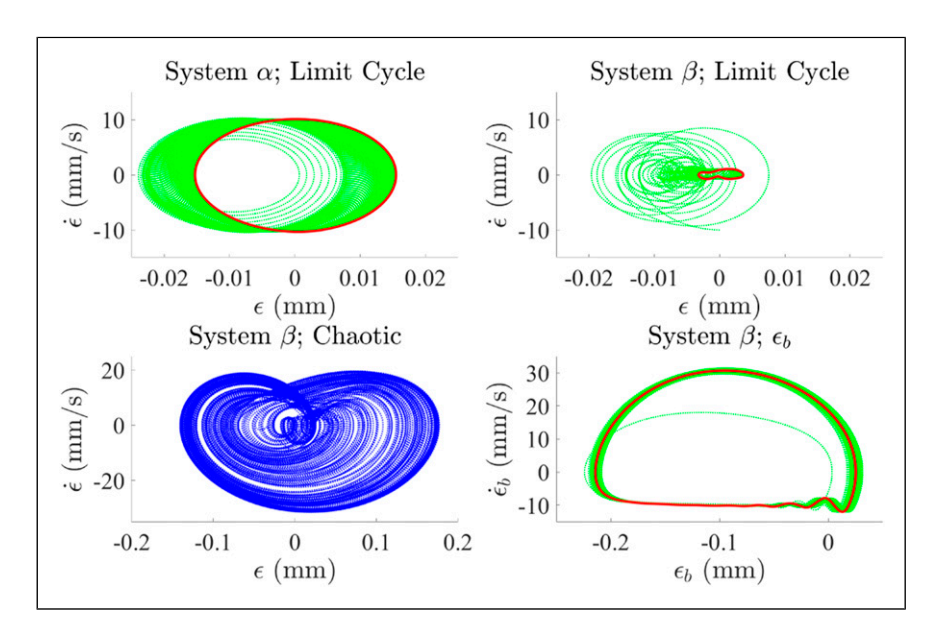


Figure 13. Phase portraits with limit cycles highlighted in solid red lines, where the control gains are (1) system α , limit cycle - $k_i = 1 \times 10^6$ N/ms, $k_p = 6.5 \times 10^5$ N/m, $k_d = 20$ Ns/m; (2) system β , limit cycle - $k_i = 1 \times 10^6$ N/ms, $k_p = 6.5 \times 10^5$ N/m, $k_d = 20$ Ns/m; (3) system β , chaotic - $k_i = 8 \times 10^6$ N/ms, $k_p = 2 \times 10^4$ N/m, $k_d = 2 \times 10^2$ Ns/m; and (4) system β , $\epsilon b - k_i = 1 \times 10^7$ N/ms, $k_p = 2 \times 10^4$ N/m, $k_d = 2 \times 10^2$ Ns/m.

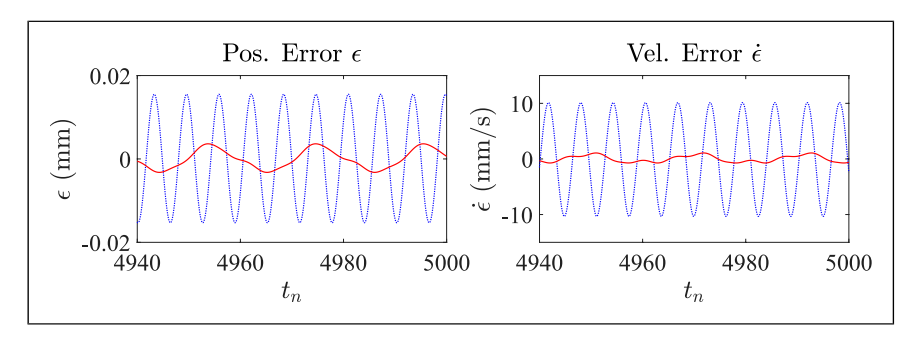


Figure 14. Comparison of limit cycle time trajectories, where - (1) dot: system α , and (2) solid: system β . The proportional–integral–derivative control gains for both systems are selected as $k_i = 1 \times 10^6$ N/ms, $k_b = 6.5 \times 10^5$ N/m, and $k_d = 20$ Ns/m.

amplitudes of limit cycles in the friction oscillator with LuGre dynamics (which is equivalent to System α). Therefore, phase portraits of the systems under different control gains are compared in Figure 13. In the limit cycle subfigures, the same parameters are used for Systems α and β . Note that the limit cycle amplitude of System β is significantly smaller than that of System α . The corresponding time domain data of \in and $\dot{\epsilon}$ are also plotted in Figure 14. This shows that the introduction of FI can reduce the amplitude of friction-induced vibration, thus agreeing with the previous experimental studies (Dong et al., 2017; Dong and Okwudire, 2018). Sub-Figure (3) illustrates that chaotic behavior may be observed with certain parameters in the presence of FI, and sub-Figure (4) demonstrates the limit cycle of the bearing states \in_b , where the stick–slip effect can be easily noticed.

The numerical study has presented many interesting observations about the characteristics of the systems. While these results are in agreement with the stability analysis, many nonlinear features of the system, such as the cause of chaotic behaviors and the reduction of limit cycle amplitudes with the FI, will need further study using nonlinear analysis.

5. Conclusion and future work

This article analytically and numerically examined the influence of friction isolator on the dynamics of a PID-controlled motion stage under the LuGre friction dynamics. Linear stability analysis was performed at the slipping equilibrium point of the systems. The eigenvalues and stability of the system were parametrically studied with respect to the PID control gains, FI design parameters, and friction parameters. Then, the numerical analysis was carried out, which validated the analytical results from linear stability analysis, and provided further insights into the nonlinear behavior of the system. The main results are as follows:

1. The effects of the friction parameters on the stability of the system with FI share similar characteristics as that without FI. Unless a very large integral gain is

- used, the stability of the system under the PID controller is dominated by the proportional and derivative gains.
- 2. Friction isolator can increase the stability region. Large $k_{\rm FI}$ or $c_{\rm FI}$ may lead to larger regions for stable PID gain selection, in particular, allowing larger stable k_i to be paired with small k_p and k_d for faster steady-state error convergence. Raising $c_{\rm FI}$ and lowering k_i also allow a more flexible table-bearing mass ratio and larger payload capacity.
- The numerical examples show that FI can reduce the amplitudes of limit cycles and prevent unbounded error, hence improve the precision of the motion stage.

The findings in this work also lay the foundation for future investigations, which include the experimental validation of the dynamical analysis results, the nonlinear analysis of the motion stage that features the nonlinear FI stiffness and the friction model, and the optimization of FI design parameters for better performance and stability of the motion stage.

Declaration of Conflicting Interests

The author(s) declared no potential conflicts of interest with respect to the research, authorship, and/or publication of this article.

Funding

The author(s) disclosed receipt of the following financial support for the research, authorship, and/or publication of this article: This work is funded by National Science Foundation (NSF) Award (CMMI #1855390 and CMMI #1855354): Towards a Fundamental Understanding of a Simple, Effective, and Robust Approach for Mitigating Friction in Nanopositioning Stages.

ORCID iDs

Jiamin Wang https://orcid.org/0000-0003-4133-9388 Xin Dong https://orcid.org/0000-0001-7872-6846

References

Al-Bender F and Swevers J (2008) Characterization of friction force dynamics. *IEEE Control Systems Magazine* 28(6): 64–81.

Altintas Y, Verl A, Brecher C, et al. (2011) Machine tool feed drives. *CIRP annals* 60(2): 779–796.

- Armstrong-Hélouvry B, Dupont P and De Wit CC (1994) A survey of models, analysis tools and compensation methods for the control of machines with friction. *Automatica* 30(7): 1083–1138.
- Bisoffi A, Da Lio M, Teel AR, et al. (2017) Global asymptotic stability of a pid control system with coulomb friction. *IEEE Transactions on Automatic Control* 63(8): 2654–2661.
- Chong S-H and Sato K (2010) Practical controller design for precision positioning, independent of friction characteristic. *Precision Engineering* 34(2): 286–300.
- De Wit CC, Olsson H, Astrom KJ, et al. (1995) A new model for control of systems with friction. *IEEE Transactions on automatic control* 40(3): 419–425.
- di Bernardo M, Kowalczyk P and Nordmark A (2003) Sliding bifurcations: a novel mechanism for the sudden onset of chaos in dry friction oscillators. *International journal of Bifurcation* and chaos 13(10): 2935–2948.
- Dong X, Liu X, Yoon D, et al. (2017) Simple and robust feedforward compensation of quadrant glitches using a compliant joint. CIRP Annals 66(1): 353–356.
- Dong X, Okwudire C, Wang J, et al. (2019) On the friction isolator for precision motion control and its dynamics. In: ASME 2019 international design engineering technical conferences and computers and information in engineering conference, California, USA, 18–21, August, 2019: American Society of Mechanical Engineers Digital Collection..
- Dong X and Okwudire CE (2018) An experimental investigation of the effects of the compliant joint method on feedback compensation of pre-sliding/pre-rolling friction. *Precision Engineering* 54: 81–90.
- Duffour P and Woodhouse J (2004) Instability of systems with a frictional point contact. part 1: basic modelling. *Journal of Sound and Vibration* 271(1–2): 365–390.
- Feeny BF and Liang JW (1997) Phase-space reconstructions and stick-slip. *Nonlinear Dynamics* 13(1): 39–57.
- Futami S, Furutani A and Yoshida S (1990) Nanometer positioning and its micro-dynamics. *Nanotechnology* 1(1): 31.
- Galvanetto U (1999) Non-linear dynamics of multiple friction oscillators. Computer methods in applied mechanics and engineering 178(3–4): 291–306.
- Hensen RHA, Van de Molengraft MJG and Steinbuch M (2003) Friction induced hunting limit cycles: a comparison between the lugre and switch friction model. *Automatica* 39(12): 2131–2137.
- Hinrichs N, Oestreich M and Popp K (1998) On the modelling of friction oscillators. *Journal of sound and Vibration* 216(3): 435–459.
- Hoffmann N (2007) Linear stability of steady sliding in point contacts with velocity dependent and lugre type friction. *Journal of Sound and Vibration* 301(3–5): 1023–1034.
- Hoffmann N, Fischer M, Allgaier R, et al. (2002) A minimal model for studying properties of the mode-coupling type instability in friction induced oscillations. *Mechanics Research Communications* 29(4): 197–205.
- Johanastrom K and Canudas-De-Wit C (2008) Revisiting the lugre friction model. *IEEE Control Systems* 28(6): 101–114.
- Kempf CJ and Kobayashi S (1999) Disturbance observer and feedforward design for a high-speed direct-drive positioning

- table. IEEE Transactions on control systems Technology 7(5): 513–526.
- Khalil HK (2002) Nonlinear Systems. Upper Saddle River, NJ: Prentice Hall.
- Kim HM, Park SH and Han SI (2009) Precise friction control for the nonlinear friction system using the friction state observer and sliding mode control with recurrent fuzzy neural networks. *Mechatronics* 19(6): 805–815.
- Kim M-S and Kim J-H (2011) Design of a gain scheduled pid controller for the precision stage in lithography. *International Journal of precision engineering and manufacturing* 12(6): 993–1000
- Kruse S, Tiedemann M, Zeumer B, et al. (2015) The influence of joints on friction induced vibration in brake squeal. *Journal of Sound and Vibration* 340: 239–252.
- Li Z, Ouyang H and Guan Z (2016) Nonlinear friction-induced vibration of a slider-belt system. *Journal of Vibration and Acoustics* 138(4): 041006.
- Marques F, Flores P, Pimenta Claro JC, et al. (2016) A survey and comparison of several friction force models for dynamic analysis of multibody mechanical systems. *Nonlinear Dy-namics* 86(3): 1407–1443.
- Nakano K and Maegawa S (2009) Stick-slip in sliding systems with tangential contact compliance. *Tribology International* 42(11–12): 1771–1780.
- Niknam A and Farhang K (2019) Friction-induced vibration in a two-mass damped system. *Journal of Sound and Vibration* 456: 454–475.
- Oestreich M, Hinrichs N and Popp K (1996) Bifurcation and stability analysis for a non-smooth friction oscillator. *Archive of Applied Mechanics* 66(5): 301–314.
- Ogata K (2010) *Modern control engineering*. 5th edition. Upper Saddle River: Pearson.
- Pascal M (2017) Periodic motions with overshooting phases of a two-mass stick-slip oscillator. *Journal of Computational and Nonlinear Dynamics* 12(4): 044504.
- Ren B, San PP, Ge SS, et al. (2008) Robust adaptive control of hard disk drives with hysteresis friction nonlinearity in mobile applications. *IFAC Proceedings Volumes* 41(2): 2538–2543.
- Saha A and Wahi P (2011) Delayed feedback for controlling the nature of bifurcations in friction-induced vibrations. *Journal of* sound and vibration 330(25): 6070–6087.
- Saha A, Wahi P, Wiercigroch M, et al. (2016) A modified lugre friction model for an accurate prediction of friction force in the pure sliding regime. *International Journal of Non-Linear Mechanics* 80: 122–131.
- Sariyildiz E, Oboe R and Ohnishi K (2019) Disturbance observerbased robust control and its applications: 35th anniversary overview. *IEEE Transactions on Industrial Electronics* 67(3): 2042–2053
- Van de Vrande BL, Van Campen DH and De Kraker A (1999) An approximate analysis of dry-friction-induced stick-slip vibrations by a smoothing procedure. *Nonlinear Dynamics* 19(2): 159–171.
- Zheng M, Zhou S and Tomizuka M (2017) A design methodology for disturbance observer with application to precision motion control: an h-infinity based approach. In: 2017 American control conference (ACC), Seattle, WA, 24–26 May 2017, Seattle, WA: IEEE, pp. 3524–3529.